

# 2021 CEDAR poster competition

- ❑ 136 posters were presented and 72 student posters in competition among them 14 undergraduates.
- ❑ The students presented from the US, Brazil, China, Germany, Peru, Taiwan, India, & Iran.
- ❑ Posters were presented at 3 days and for each days the poster winners were selected by the poster judges.
- ❑ Thanks to all the student presenting a poster at CEDAR

# Special thanks to the judges:

*Brian Harding, Xuguang Cai, Phil Richards, Lindsay Goodwin, Scott England, Meghan Burleigh, Aramesh Seif, Qingyu Zhu, Federico Gasperini, D Selvaraj, Steve Kaeppler, Shantanab Debchoudhur, Chihoko Cullens, Rafael Mesquita, Joshua Petit, Mack Jones, Luis Navarro, Leslie Lamarche*

## The poster judging committee:

Julio Urbina (chair), Liying Qian, Jens Oberheide, Asti Bhatt, Jonathan Snively

# Criteria to select poster winners

- Two members of the CEDAR CSSC facilitated the discussion but did not vote.
- Every poster received two scores: round 1 score (500 points max) and round 2 score (500 points max). These two scores were added. The judges discussed the scores and selected the best 8 posters out of this pool.
- The judges discussed these 8 posters further and selected the first place in the competition.
- The remaining best 7 posters were then discussed to select the second place.
- If an undergraduate poster made it to the top 8 and there was more than one undergraduate in the competition, an honorable mention was chosen.

# Day 1: 2<sup>nd</sup> Prize

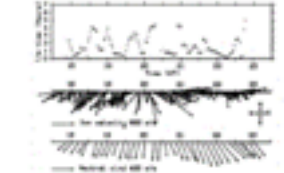
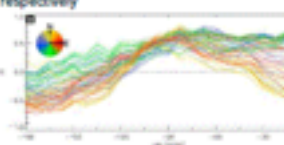
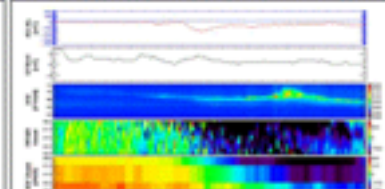
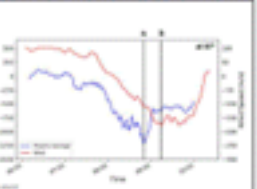
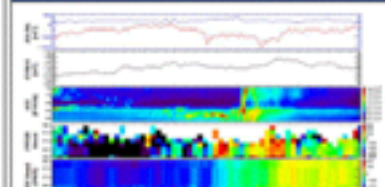
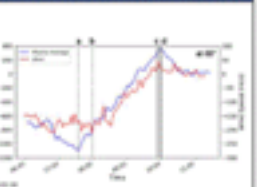


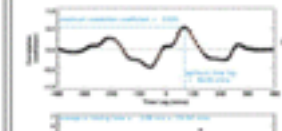

Katherine Davidson  
University of Alabama, Huntsville

Title:  
Investigating Ionosphere-  
Thermosphere Coupling in the  
Nightside Auroral Oval

## Investigating Ionosphere-Thermosphere Coupling in the Nightside Auroral Oval

Katherine Davidson<sup>1</sup>, Ying Zou<sup>1</sup>, Mark Conde<sup>2</sup>, Roger Varney<sup>3</sup>, Stephen Mendon<sup>4</sup>

<sup>1</sup>Department of Space Science, The University of Alabama in Huntsville, Huntsville, AL, USA, <sup>2</sup>Department of Physics, University of Alaska Fairbanks, Fairbanks, AK, USA, <sup>3</sup>IGR International, Menlo Park, CA, USA, <sup>4</sup>Space Sciences Laboratory, University of California, Berkeley, CA, USA

Background & Motivation	Quiet Time Event - 2013 Mar 07
<ul style="list-style-type: none"><li>Ionospheric plasma convection is governed by electromagnetic coupling to the magnetosphere and solar wind</li><li>The neutral atmosphere in the auroral oval has a number of drivers, but is mostly dominated by ion drag and thermal pressure gradients</li><li>The response of the neutral wind to changes in plasma flow is reported to have a wide range of variability (as low as tens of minutes), and the controlling factors are not well characterized</li></ul>  <p>Figure 1: E-folding time, ion velocity vector and neutral wind vector on 14 November 2008. (Joshi et al., 2015)</p> <ul style="list-style-type: none"><li>Kosch et al., 2001 found that the ion-neutral coupling time constant averaged 1.8 and 3.3 hours for a geomagnetically active and quiet period, respectively</li></ul>  <p>Figure 2: Time-lagged correlation analysis on plasma flow and neutral wind on 1 December 2013. (Joshi et al., 2015)</p> <ul style="list-style-type: none"><li>Billett et al., 2010 performed a time-lagged correlation analysis and found the neutral lag time to be ~75 minutes</li></ul> <p style="text-align: center;"><b>Motivation</b></p> <p>Studying how neutral wind responds to changes in the plasma flow will show the strength of the coupling between the two species.</p>	<p style="text-align: center;">Quiet Time Event - 2013 Mar 07</p>  <p>Figure 3: Summary of the 2013 Mar 07 event, including AE, ASI and ion velocity vector, neutral wind vector and ASI data.</p>  <p>Figure 4: Time series plot of ion velocity and neutral wind on 07 Mar 2013.</p> <ul style="list-style-type: none"><li>Plasma turns from stationary to westward flow at ~01:40UT, simultaneously with a spike of AE and presence of an east-west arc in ASI data</li><li>Neutral wind also turns from an eastward to westward flow</li><li>The times at which plasma and wind reach their minimums are plotted as (a) and (b), respectively, on the time series plot</li><li>The time difference between these minimums, or the response time, is ~25 minutes</li></ul>
	Storm Time Event - 2016 Feb 18
	<p style="text-align: center;">Storm Time Event - 2016 Feb 18</p>  <p>Figure 5: Summary of the 2016 Feb 18 event, including ion velocity vector, neutral wind vector and ASI data.</p>  <p>Figure 6: Time series plot of ion velocity and neutral wind on 18 Feb 2016.</p> <ul style="list-style-type: none"><li>Plasma turns from a strong westward flow to an eastward flow after AE dropped at around 03:00UT</li><li>Neutral wind follows the plasma, turning from a westward to eastward flow</li><li>The times at which the plasma and wind start to turn are plotted as (a) and (b), respectively</li><li>Additionally, the times at which plasma and wind reach their maximums are plotted as (c) and (d), respectively</li><li>The time difference between the flow change is ~25 minutes, and the time difference between the maximums is ~8 minutes</li></ul>
Instrumentation	Conclusions
<ul style="list-style-type: none"><li>THEMIS All Sky Imagers (ASI): FYXN, GAKD, INUV</li><li>Scanning Doppler Imagers (SDI): PYR, TLK</li><li>Poker Flat Incoherent Scatter Radar (PFISR)</li></ul>  <p>Figure 7: ASI locations over Alaska</p>  <p>Figure 8: PFISR location</p>	<ul style="list-style-type: none"><li>Both events show a response time of &lt; 30 mins, shorter than what has previously been shown</li><li>Initially, both the quiet and active time event have around the same response time</li><li>As AE continues to increase, the storm time event becomes more strongly coupled and has a response time of &lt; 10 minutes</li></ul>  <p>Figure 9: A correlation of the time-lagged correlation analysis to the e-folding time for 13 Mar 2013. (Joshi et al., 2015)</p> <ul style="list-style-type: none"><li>In the future, a time-lagged correlation analysis and e-folding time calculation will be performed</li><li>Comparing an observation vs. theory response time will provide information about the importance of ion-drag as a driver of the neutral atmosphere [Joshi et al., 2015]</li><li>These response times will then be compared across geomagnetic activity levels to see how the effects of ion-drag change with varying levels of activity</li></ul> 

# Day 1: 1st Prize

Lance Davis  
University of New Hampshire

Title:  
Probing the Density Profile of the Thermosphere Using Loss Cone Measurements

## Probing the Density Profile of the Thermosphere Using Loss Cone Measurements

L. A. Davis\* and J. H. Clemmons  
University of New Hampshire  
\*Corresponding Author: lad1040@wildcats.unh.edu

### Introduction

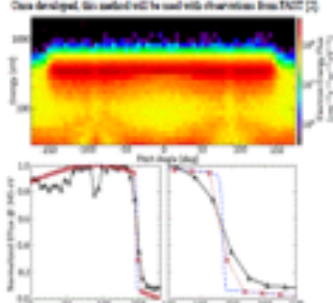
The thermosphere is the region of Earth's neutral atmosphere (~80-1000 km altitude) where both neutral gas processes and interactions between the neutral gas and the plasma of the ionosphere occur. This region is key to understanding how the neutral atmosphere couples to the ionosphere, the magnetosphere, and the space environment.

Traditional loss cone is a novel, mass-saving method for probing the altitudinal structure of the high-latitude thermosphere using loss cone measurements from a satellite. Current methods, providing useful insights as to the study of the thermosphere, have limitations, such as being fixed in location (such as ground-based observations), having a limited number of discrete altitudes (such as sounding rocket ascents), and averaging over latitudinal and longitudinal distributions due to averaging along the line of sight (such as the limb-scanning technique of GOSWAMI [1]). This new method would complement current methods by providing a large database with full spatial resolution.

Our application of this method is studying how the altitudinal structure of the thermosphere responds to geomagnetic activity and solar cycle. Due to a satellite being particle distribution measurements, the response can be also be analyzed as a function of geomagnetic conditions and time.

### Fast Auroral Snapshot (FAST) Explorer

Once developed, this method will be used with observations from FAST [2].



(Top) FAST Explorer satellite. (Bottom Left) One of the particle distribution at 340 eV with the simulated. (Bottom Right) Zoom-in of the loss cone slope compares our model (blue) to FAST (black) observations. Scattered at the same angular resolution as FAST (4e), our model better correlates. Further work is needed to improve the agreement between this model and real observations, and how the better distribution for model.

FAST is well suited to utilize this method:

- Burst mode distribution measurements occur frequently
- FAST's close approach, polar orbit allows for remote sensing of the high-latitude thermosphere and a large loss cone with many sampling points along the loss cone slope
- The mission duration (1991 to 2009) provides a large, multi-decade, which corresponds to at least 22 geomagnetic storms [3]

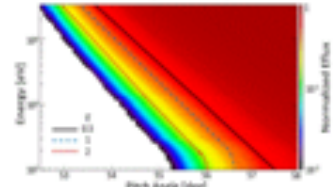
The Electron Spectroscopic Analyser (ESA) [4] is an appropriate instrument:

- 40 energy bins in the range of interest (~100 eV)
- Angular resolution is  $\sim 10^\circ$  and the sampling rate is 70 Hz
- Combining the ESA distributions with the SESAR 1.6 ms sampling rate, angular resolutions of  $\sim 7^\circ$  can be reached

Given these characteristics, FAST's particle distribution will provide  $\sim 1.6$  data points per pitch angle bin.

### Novel Method Description

Particle distribution was modeled by using particles along a dipole magnetic field and using the HELMHOFF (H) model [5] to model the distribution of the neutral gas in the thermosphere.

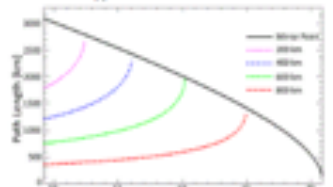


A modeled particle distribution with the energy range and resolution of FAST, with the energy bin associated, for a set altitude. The energy dependence of the loss cone angle width can be seen, ranging from  $\sim 10^\circ$  to  $70^\circ$ .

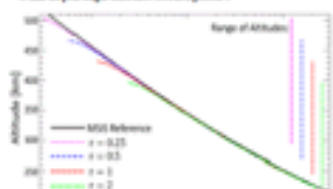
The most interesting cross-section for gas species [6] depend on particle energy, increasing with increasing energy. The optical depth  $\tau$  is given by:

$$\tau = \int_{r_0}^{r} n(r) \sigma(r) dr \quad (1)$$

where  $r$  is the path length (dependent on altitude,  $r$  is the neutral density), and  $r_0$  is the total cross-section for energy  $E$ . Using Equation 1, as well as the observed attenuation of the flux (optical depth), path lengths, and cross-section, the density profile can be calculated.



Particle distribution provide the total optical depth measured to a particular pitch angle and this also altitude. To find the density in the altitude range between two data points, the difference in optical depth is taken. The plot shows shows how, for a given pitch angle, the path length measured depends on altitude (indicated arrows) up to the current point (black). This is the way used to find the path length difference used in Equation 1.

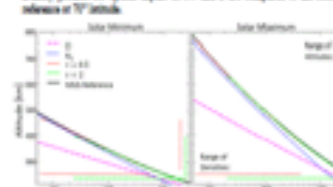


As an example another density profile calculation is shown above. For comparison, the GOSWAMI data used for this calculation is shown as black. The different lines correspond to different optical depths. A wide range of altitudes are probed, covering several scale heights. If FAST observations were used, there would be  $\sim 1$  data points per scale height.

### Results

#### Solar Cycle Results:

Comparing the altitudinal structure during solar maximum and minimum. Density profiles for optical depths of 0.1 and 1 are compared to the GOSWAMI reference at 70° altitude.

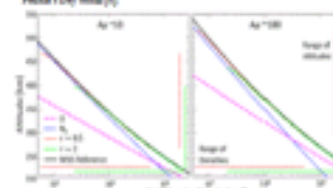


#### Solar Cycle Observations:

- Due to higher energy input during solar maximum, the thermosphere expands, thus reducing the loss cone angle width and increasing the range of altitudes probed.
- For both solar maximum and minimum, this method probes densities over  $\sim 2$  orders of magnitude, roughly 4 scale heights.
- Lower energies (near the optical depth profiles, i.e.,  $\sim 100$  eV for  $\tau = 1$ ) correspond to regions the same density regardless of solar activity, possible use for calibrating the method.

#### Geomagnetic Activity Results:

Comparing the altitudinal structure over before and after the onset of a geomagnetic storm. The storm was simulated after the intense ( $Dst \sim -240$ ) St. Patrick's Day event [8].



#### Geomagnetic Storm Observations:

- The change in the altitude probed between storm onset and the main phase is less than between solar maximum and minimum.
- The range of altitudes probed, covering  $\sim 1$  scale heights, does not change significantly with geomagnetic activity.

#### Overall:

This method can probe  $\sim 1$  scale heights regardless of solar cycle or geomagnetic conditions. The range of altitudes probed is more variable, for example ranging from  $\sim 270$ -700 km for solar maximum to  $\sim 350$ -600 km for solar minimum.

### Further Considerations

- Account for Other Phenomena:
  - Field-aligned potential drops below the spacecraft ionosphere electrons, affecting the loss cone and particle trajectories [7]
  - Electron drift away while traveling along the field line, thus changing the cross-section value
  - Plasma ionospheric electron profiles variations and other, either of which may occur to and be observed by the satellite
- Improvements to the Model used for the Method Development:
  - Improve the IOST of Earth's magnetic field model [9]
  - Utilize Electron Drifters Model (e.g., [10]) to show particle trajectories and account for phenomena below the spacecraft
- Understanding Satellite Observation Limitations:
  - Influence of angle resolution on quality of density profile
  - Using a high sampling frequency and loss cone mapping to improve angular resolution
  - Dependence on the number of observations points per scale height as the number of energy bins
  - Impact of orbital radius on observed loss cone size

### Summary and Future Work

**Key Points:**

- This novel, mass-saving method probes the altitudinal structure of the high-latitude thermosphere over  $\sim 4$  scale heights with  $\sim 1$  observation point each
- Since the angle width of the loss cone is energy dependent and thus also altitude dependent, the structure of the flux can be used to calculate a density profile
- FAST particle distribution observations, combined with this method, can be used to view the altitudinal structure as a function of latitude and longitude

**Future Work:**

- Accounting for phenomena, such as field-aligned potential drops, that occur below the spacecraft and affect the loss cone
- Finalize the development of this novel method and apply it to the particle distributions from FAST
- Show how the altitudinal structure of the thermosphere at high latitudes ( $> 70^\circ$ ) respond to geomagnetic forcing
- Show how the structure of the thermosphere vary and evolve during geomagnetic storms as a function of time and position

### References

- GOSWAMI, B. N., 1974, *Journal of Geophysical Research*, **79**, 10, 5913-5920.
- FAST Explorer, <http://www.unh.edu/~fast/>
- CHAPMAN, G. M., 1969, *Journal of Geophysical Research*, **74**, 10, 2685-2690.
- CHAPMAN, G. M., 1970, *Journal of Geophysical Research*, **75**, 10, 2105-2110.
- CHAPMAN, G. M., 1971, *Journal of Geophysical Research*, **76**, 10, 2405-2410.
- CHAPMAN, G. M., 1972, *Journal of Geophysical Research*, **77**, 10, 2705-2710.
- CHAPMAN, G. M., 1973, *Journal of Geophysical Research*, **78**, 10, 2805-2810.
- CHAPMAN, G. M., 1974, *Journal of Geophysical Research*, **79**, 10, 2905-2910.
- CHAPMAN, G. M., 1975, *Journal of Geophysical Research*, **80**, 10, 3005-3010.
- CHAPMAN, G. M., 1976, *Journal of Geophysical Research*, **81**, 10, 3105-3110.
- CHAPMAN, G. M., 1977, *Journal of Geophysical Research*, **82**, 10, 3205-3210.
- CHAPMAN, G. M., 1978, *Journal of Geophysical Research*, **83**, 10, 3305-3310.
- CHAPMAN, G. M., 1979, *Journal of Geophysical Research*, **84**, 10, 3405-3410.
- CHAPMAN, G. M., 1980, *Journal of Geophysical Research*, **85**, 10, 3505-3510.
- CHAPMAN, G. M., 1981, *Journal of Geophysical Research*, **86**, 10, 3605-3610.
- CHAPMAN, G. M., 1982, *Journal of Geophysical Research*, **87**, 10, 3705-3710.
- CHAPMAN, G. M., 1983, *Journal of Geophysical Research*, **88**, 10, 3805-3810.
- CHAPMAN, G. M., 1984, *Journal of Geophysical Research*, **89**, 10, 3905-3910.
- CHAPMAN, G. M., 1985, *Journal of Geophysical Research*, **90**, 10, 4005-4010.
- CHAPMAN, G. M., 1986, *Journal of Geophysical Research*, **91**, 10, 4105-4110.
- CHAPMAN, G. M., 1987, *Journal of Geophysical Research*, **92**, 10, 4205-4210.
- CHAPMAN, G. M., 1988, *Journal of Geophysical Research*, **93**, 10, 4305-4310.
- CHAPMAN, G. M., 1989, *Journal of Geophysical Research*, **94**, 10, 4405-4410.
- CHAPMAN, G. M., 1990, *Journal of Geophysical Research*, **95**, 10, 4505-4510.
- CHAPMAN, G. M., 1991, *Journal of Geophysical Research*, **96**, 10, 4605-4610.
- CHAPMAN, G. M., 1992, *Journal of Geophysical Research*, **97**, 10, 4705-4710.
- CHAPMAN, G. M., 1993, *Journal of Geophysical Research*, **98**, 10, 4805-4810.
- CHAPMAN, G. M., 1994, *Journal of Geophysical Research*, **99**, 10, 4905-4910.
- CHAPMAN, G. M., 1995, *Journal of Geophysical Research*, **100**, 10, 5005-5010.
- CHAPMAN, G. M., 1996, *Journal of Geophysical Research*, **101**, 10, 5105-5110.
- CHAPMAN, G. M., 1997, *Journal of Geophysical Research*, **102**, 10, 5205-5210.
- CHAPMAN, G. M., 1998, *Journal of Geophysical Research*, **103**, 10, 5305-5310.
- CHAPMAN, G. M., 1999, *Journal of Geophysical Research*, **104**, 10, 5405-5410.
- CHAPMAN, G. M., 2000, *Journal of Geophysical Research*, **105**, 10, 5505-5510.
- CHAPMAN, G. M., 2001, *Journal of Geophysical Research*, **106**, 10, 5605-5610.
- CHAPMAN, G. M., 2002, *Journal of Geophysical Research*, **107**, 10, 5705-5710.
- CHAPMAN, G. M., 2003, *Journal of Geophysical Research*, **108**, 10, 5805-5810.
- CHAPMAN, G. M., 2004, *Journal of Geophysical Research*, **109**, 10, 5905-5910.
- CHAPMAN, G. M., 2005, *Journal of Geophysical Research*, **110**, 10, 6005-6010.
- CHAPMAN, G. M., 2006, *Journal of Geophysical Research*, **111**, 10, 6105-6110.
- CHAPMAN, G. M., 2007, *Journal of Geophysical Research*, **112**, 10, 6205-6210.
- CHAPMAN, G. M., 2008, *Journal of Geophysical Research*, **113**, 10, 6305-6310.
- CHAPMAN, G. M., 2009, *Journal of Geophysical Research*, **114**, 10, 6405-6410.
- CHAPMAN, G. M., 2010, *Journal of Geophysical Research*, **115**, 10, 6505-6510.
- CHAPMAN, G. M., 2011, *Journal of Geophysical Research*, **116**, 10, 6605-6610.
- CHAPMAN, G. M., 2012, *Journal of Geophysical Research*, **117**, 10, 6705-6710.
- CHAPMAN, G. M., 2013, *Journal of Geophysical Research*, **118**, 10, 6805-6810.
- CHAPMAN, G. M., 2014, *Journal of Geophysical Research*, **119**, 10, 6905-6910.
- CHAPMAN, G. M., 2015, *Journal of Geophysical Research*, **120**, 10, 7005-7010.
- CHAPMAN, G. M., 2016, *Journal of Geophysical Research*, **121**, 10, 7105-7110.
- CHAPMAN, G. M., 2017, *Journal of Geophysical Research*, **122**, 10, 7205-7210.
- CHAPMAN, G. M., 2018, *Journal of Geophysical Research*, **123**, 10, 7305-7310.
- CHAPMAN, G. M., 2019, *Journal of Geophysical Research*, **124**, 10, 7405-7410.
- CHAPMAN, G. M., 2020, *Journal of Geophysical Research*, **125**, 10, 7505-7510.
- CHAPMAN, G. M., 2021, *Journal of Geophysical Research*, **126**, 10, 7605-7610.
- CHAPMAN, G. M., 2022, *Journal of Geophysical Research*, **127**, 10, 7705-7710.
- CHAPMAN, G. M., 2023, *Journal of Geophysical Research*, **128**, 10, 7805-7810.
- CHAPMAN, G. M., 2024, *Journal of Geophysical Research*, **129**, 10, 7905-7910.
- CHAPMAN, G. M., 2025, *Journal of Geophysical Research*, **130**, 10, 8005-8010.

# Day 2: Honorable mention Undergraduate

Jhassmin Aricoché

Radio Observatorio de Jicamarca,  
Instituto Geofísico del Perú, Lima,  
Perú

Title:  
Modeling ionograms with deep  
neural networks: Application to  
foF2 forecasting

**Modeling ionograms with deep neural networks: Applications to foF2 forecasting**  
J. Aricoché<sup>1,2</sup>, E. Rojas<sup>1</sup>, M. Milla<sup>3</sup>  
<sup>1</sup>Radio Observatorio de Jicamarca, Instituto Geofísico del Perú, Lima, Perú  
<sup>2</sup>Universidad Nacional del Centro del Perú, Perú  
<sup>3</sup>Cornell University, New York, USA

**Abstract**  
The ionosphere state parameters are of fundamental importance not only for radio communication but also for space weather. As most of the space phenomena, the dynamics are governed by nonlinear processes that make forecasting a challenging endeavor. We now have available enormous datasets and ubiquitous experimental sources that can help us finding the intricate regularities in these phenomena. In this work, we will focus on the forecasting of some parameters of the steady-state ionosphere. We used ionograms from Jicamarca Radio Observatory digsonds to train two neural networks. We produced forecasts of ionospheric parameters such as virtual heights and foF2 using this consideration ionogram characteristics. These estimations were compared to the corresponding values obtained from the digsonds, the persistence model, and foF2 values obtained from the International Reference Ionosphere.

**1. Scientific problem and background**  
Initially, this work was developed as part of our main research project which aims to estimate electron densities while forecasting ionograms. Ionograms are states of representation of the ionosphere at a given time and whose defined traces can be identified through the use of neural networks [1]. However, we noticed that we were applying a novel method to predict ionograms and foF2, which results will be shown in this poster.  
There were several approaches to estimate foF2 by using foF2 time series data, geophysical data, and neural networks as presented in [2]. However these methods did not use ionograms to make foF2 predictions.  
In this work, not only foF2, geophysical parameters and time are used to find this important value for ionogram predictions. But also, frequencies that are not foF2 and their virtual heights are used to let a multi-layer perceptron neural network classify and help us to find foF2.

**2. Datasets**  
Digsonds ionograms used to train the model were filtered by the c-level flag provided by AIRIS7. c-level flag indicates and qualifies some of the AIRIS7 scaled results [3]. It indicates high quality and 10 low quality ionograms labeled with 1 were taken.  
3 years and five months (2012 - May 2016) from 10 am to 6:00 pm UT hours were considered to train the model.

**3. Model architecture**  
We chose neural networks architecture based on experience and multiple tests.  
Figure 1 shows regression-like architecture to predict and capture ionograms shape. Sigmoid activation functions were used.  
Figure 2 shows binary classification-like architecture to find which frequencies of the given are not foF2 and are below foF2. Thereby we used the information to identify which are foF2. Sigmoid activation functions were used.

**4. Samples predictions and comparisons**  
Figure 3 shows ionogram prediction, its prediction errors, digsonds ionograms, and persistence models.  
Traces for lower and higher frequencies were extrapolated by the neural network, however, extrapolated virtual heights for the higher frequencies were reduced by the binary classification neural network that helps us to identify which frequencies are foF2. In some tests we did not consider steps of anomaly (20 June of 2016).  
Figure 4 shows foF2 predictions of the NN, foF2 of digsonds and foF2 digsonds values for the ionograms.  
Figure 5 shows foF2 prediction errors obtained with NN model and the foF2 digsonds predictions.

**5. Conclusions**  
Neural networks model can capture geophysical parameters and virtual heights variations to show foF2 results slightly better than-IRI estimations.  
Ionogram estimations that adjust to the ionogram's common shape were predicted for eight months.  
By using not only frequencies that are foF2 but also frequencies that are not and virtual heights to estimate foF2, we can observe that this approach looks like a promising application for small observatories made with a neural network that are not based on ionometry, which implies it is a less complex approach. However, more training with more data should be made to make affirmations.

**6. Future works**  
There are available 30 years of ionogram data at Jicamarca Radio Observatory provided by the digsonds. Thus, more training will be needed and of course will be include.  
To evaluate this performance new IRI93 comparison will be made.  
After accurate ionogram predictions have been obtained, future work will be oriented toward electron density forecasting.

**7. Acknowledgments**  
Thanks to Jicamarca Radio Observatory and Instituto Geofísico del Perú staff.

**8. References**  
[1] J. Aricoché, E. Rojas, and M. Milla, "Modeling ionograms with deep neural networks: Application to foF2 forecasting," in *2021 IEEE International Conference on Systems, Man, and Cybernetics (SMC)*, 2021, pp. 1111-1116.  
[2] J. Aricoché, E. Rojas, and M. Milla, "Forecasting ionograms with deep neural networks: Application to foF2 forecasting," in *2021 IEEE International Conference on Systems, Man, and Cybernetics (SMC)*, 2021, pp. 1117-1122.  
[3] J. Aricoché, E. Rojas, and M. Milla, "Forecasting ionograms with deep neural networks: Application to foF2 forecasting," in *2021 IEEE International Conference on Systems, Man, and Cybernetics (SMC)*, 2021, pp. 1123-1128.

2021 CEDAE Virtual Meeting, June 22-26  
jhassmin.aricoche@rjy.igp.gub.pe

# Day 2: 2<sup>nd</sup> Prize

Jack Wang

University of Colorado, Boulder

Title:

Numerical study to uncover the driving mechanisms of the migrating diurnal tide day-to-day variability

**Numerical study to uncover the driving mechanisms of the migrating diurnal tide day-to-day variability**  
Jack C. Wang & Scott E. Palo, Smead Department of Aerospace Engineering Sciences, University of Colorado Boulder

**Problem Statement**  
This research aims to determine the fundamental mechanisms driving the day-to-day variability of the DW1.

**Introduction**  
DW1 can be variable over a range of scales from days to inter-annual dependence. While the causes of the long-term variability are well characterized, the driving mechanisms for the DW1 short-term variability is still an open research topic.

**Model & Methodology**  
In this study, a series of TIME-GCM control simulations are conducted to explore the possible mechanisms responsible for the DW1 day-to-day variability.

**Mean Wind & DWI Source Variability**

**Closing Remarks**

- The impact of variations in the background state and source variability on the day-to-day variability of the DW1 is explored in this study.
- Changes in the DW1 wave source forcing play a dominant role in the DW1 day-to-day variability, while the background state changes play a secondary role.
- Term analysis and correlation analysis DW1 day-to-day variability is caused by the adiabatic process of (1,1) Hough mode from the source region.
- Horizontal advection variation by the mean state changes results in the DW1 short-term variation away from the dominated (1,1) Hough mode.

**Acknowledgement**  
This research was supported by NSF grant AGS-1552286, part of the CEDAR program under the direction of Dr. Scott Palo. This work was performed while J.C.W. held a Government Scholarship for Study Abroad awarded by the Ministry of Education, Taiwan.

**DWI d2d variability by source & mean state changes**

**DWI tendency term analysis**

**Corr. Analysis with Source Forcing**

# Day 2: 1<sup>st</sup> Prize

Reza Janalizadeh  
Penn State University

Title:  
Revisiting the associative detachment reaction of nitrogen molecules with the anion of atomic oxygen in the context of gas discharges

## Revisiting the Associative Detachment Reaction of Nitrogen Molecules with the Anion of Atomic Oxygen in the Context of Gas Discharges



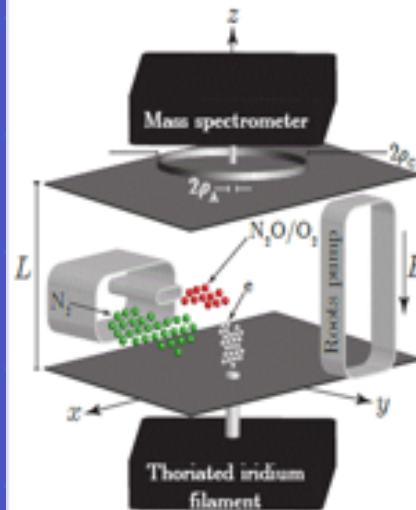
Reza Janalizadeh and Victor P. Pasko

Communications and Space Sciences Laboratory, The Pennsylvania State University, University Park, PA 16802 (reza.j@psu.edu; vpasko@psu.edu)

### 1. Abstract

Current growth measurements show negligible electron attachment in air [e.g., Moruzzi and Price, *J. Phys. D: Appl. Phys.*, vol. 7, no. 10, pp. 1434-1440, 1974]. This observation has been interpreted in terms of an electron detachment reaction, which involves molecular nitrogen,  $N_2$ , and counteracts two-body attachment of electrons to molecular oxygen,  $O_2$ . Contrary to previous studies [e.g., Hopper et al., *J. Chem. Phys.*, vol. 65, no. 12, pp. 5474-5484, 1976; Kostyl et al., *Plasma Sources Sci. Technol.*, vol. 1, no. 3, pp. 207-220, 1992; Rayment and Moruzzi [Int. J. Mass Spectrom. Ion Phys., vol. 25, no. 3, pp. 321-326, 1978] interpret their flow-drift tube results in terms of  $O^-$  collisions with ground state  $N_2$ . Here, we model the experiment in [Rayment and Moruzzi, 1978], provide corrections to the theoretical approach in that work, and interpret results in [Rayment and Moruzzi, 1978] in terms of an alternative detachment reaction which includes vibrationally excited  $N_2$ , exclusively.

### 2. Flow-Drift Tube in [Rayment and Moruzzi, 1978]



Schematics of the flow-drift tube in [Rayment and Moruzzi, 1978]

### 3. Modeling Experiments in [Rayment and Moruzzi, 1978]

Detailed description of the theoretical modeling presented here may be found in [Janalizadeh and Pasko, *GRL*, 48, e2020GL091134, 2021]. Following [Rayment and Moruzzi, 1978], we assume associative detachment, dissociative attachment, and convection and diffusion of electrons and  $O^-$  ions are the only processes which occur in the flow-drift tube.

The ionic current per unit electron current may be calculated as:

$$\frac{I_i(L)}{I_e} = \alpha_a \left( \frac{\rho_A}{r_0} \right)^2 \int_{z'=0}^L \frac{a(0)}{a(z')} \frac{b(z')}{b(L)} e^{-\beta_a \rho_A (L-z')} dz'$$

where  $\alpha_a$  denotes the attachment coefficient and  $\beta_a$  denotes the detachment coefficient per unit pressure. Furthermore,

$$a(z) = \pi \left[ 4(D_e/\mu_e) \frac{Lz}{V} + r_0^2 \right]$$

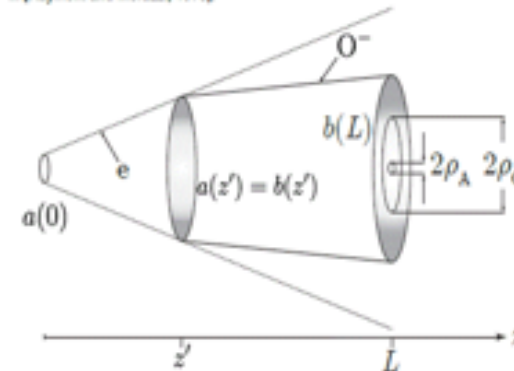
$$b(z) = a(z') + \pi \left[ 4(D_e/\mu_e) \frac{L(z-z')}{V} \right] = a(z') + \pi \left[ 0.103 \frac{L(z-z')}{V} \right]$$

in the present work. However,

$$a(z) = \pi \left[ 4(D_e/\mu_e) \frac{z^2}{V} + r_0^2 \right]$$

$$b(z) = \pi \left[ 0.103 \frac{z^2}{V} + r_0^2 \right]$$

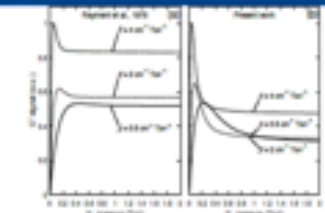
in [Rayment and Moruzzi, 1978].



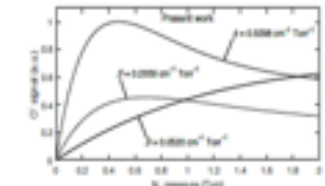
Diffusion of electrons (dashed line) and ions (solid line) along the drift gap. Here it is assumed that under the application of the electric field present in the gap, electrons travel to  $z = z'$  before  $O^-$  production through attachment. Once the  $O^-$  ion is produced it travels to the aperture at  $z = L$  unless it is destroyed through associative detachment.

Acknowledgment: This research was supported by NSF under grant AOS-2010088 to Penn State University.

### 4. Detachment due to Ground State $N_2$

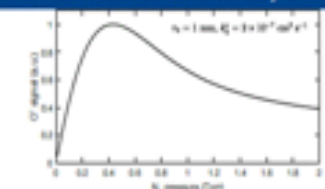


Reproduction of plots in Figure 3 of [Rayment and Moruzzi, 1978] using (a) the theoretical approach of Rayment and Moruzzi, [1978] and (b) the present work. Neither theoretical models can reproduce plots depicted in Figure 3 of [Rayment and Moruzzi, 1978] using the values of  $\beta_a$  provided in [Rayment and Moruzzi, 1978].



Reproduction of plots in Figure 3 of [Rayment and Moruzzi, 1978] using the theoretical approach of the present work and values of  $\beta_a$  consistent with rate coefficient,  $\alpha_a$  values provided in Figure 4 of [Rayment and Moruzzi, 1978].

### 5. Detachment due to Vibrationally Excited $N_2$



Reproduction of similar plots in Figure 3 of [Rayment and Moruzzi, 1978] for electron current  $I_e = 60$  nA and reduced electric field  $E/p = 20$  V/(cm Torr) using the theoretical approach of the present work under the assumption that vibrationally excited  $N_2$  is responsible for the detachment reaction, exclusively.

### 6. Conclusions

We provide corrections to the theoretical modeling in [Rayment and Moruzzi, 1978], which is the basis for the rate of the associative detachment reaction in existing modeling studies of lightning-induced upper-atmospheric discharges [e.g., Luque and Gordillo-Vazquez, *Nat. Geosci.*, vol. 5, no. 1, pp. 22-25, 2012]. More importantly, it is demonstrated that the experimental results of Rayment and Moruzzi, [1978] may be interpreted in terms of an associative detachment reaction including vibrationally excited  $N_2$ , exclusively.



# Day 3: Honorable mention Undergraduate

Alanah Cardenas-O'Toole  
University of Michigan

Title:  
Statistical and event analysis of phase and amplitude scintillations associated with polar cap patches

### Statistical and event analysis of phase and amplitude scintillations associated with polar cap patches

Alanah Cardenas-O'Toole<sup>1</sup>, Jiaen Ren<sup>1</sup>, Shasha Zou<sup>1</sup>, Jayachandran Thayyil<sup>2</sup>

<sup>1</sup>University of Michigan Department of Climate and Space Sciences and Engineering <sup>2</sup>University of New Brunswick

#### Introduction

- Ionospheric scintillation can degrade the GNSS signals and has the potential to cause a loss of access to GNSS services.
- Figure 1 shows a visual representation of the impacts of ionospheric scintillation.
- One potential source of scintillation in the high-latitude region is polar cap patches.
- Using a polar cap patch database provided by Ren et al. (2022) and scintillation data from 2022 provided by CHAN, it can be determined how polar cap patches impact ionospheric scintillation.
- It was found that statistically there is no significant phase or amplitude scintillation increases associated with patches in the polar cap, but occasionally patches do lead to enhanced scintillations. One event with enhanced scintillation was chosen for in-depth analysis and cross-comparison.

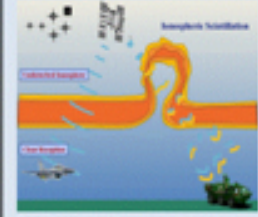


Figure 1: Representation of ionospheric scintillation. A signal path starts from a satellite and ends at a receiver on the ground. The signal path is affected by ionospheric scintillation, which is depicted as a wavy line. The signal is shown as a series of pulses, with some pulses being significantly lower in amplitude than others, indicating signal degradation.

#### Does Scintillation Increase with Patch Presence?

##### Patch Center

- Figure 2(a) shows the amplitude scintillation difference between the daily average and the 3-minute patch average. It illustrates that most differences are near or very close to zero with a longer tail on the left.
- Based on this figure, in general, the amplitude scintillation ( $S_4$ ) is not significantly impacted by the patches.
- Figure 2 (b) shows the difference between the daily average and the 3-minute average for the phase scintillation.
- The histogram is centered near zero, indicating that there is little to no difference between these values most of the time. This means that in general, the phase scintillation is not significantly impacted by patch presence.
- However, the distribution is asymmetric with a longer tail on the negative value side, which indicates that the phase scintillation within patches indeed increased in 33 events (difference < -0.20).

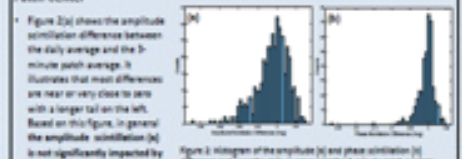


Figure 2: Histogram of the amplitude ( $S_4$ ) and phase scintillation ( $\phi$ ) difference between the daily average and the 3-minute patch average.

##### Patch Edges

- Figure 3 shows the difference between the 3-minute averaged scintillation at the leading edge of the patches and the center of the patches. The leading edge is defined as the half width of the patch that first passed RGR-N. This was done to determine if there was increased scintillation at the edges relative to the center.
- There does not appear to be a significant difference between the patch leading edges and the patch center, indicating that patch edges do not cause further enhanced scintillation than the patch center.
- We similarly looked at the trailing edge and found the same result. This indicates that the patch overall does not cause significant phase or amplitude scintillation.

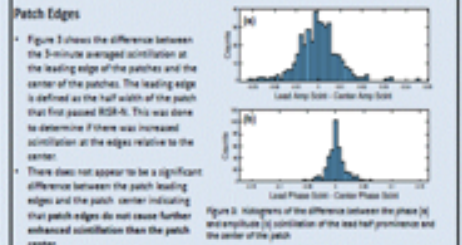


Figure 3: Histograms of the difference between the phase ( $\phi$ ) and amplitude ( $S_4$ ) scintillation of the lead half prominence and the center of the patch.

##### MUT Dependence

- Figure 4 shows a clear relationship between MUT and scintillation during polar cap patches. (a) shows the maximum value of the phase scintillation over a period of three minutes centered on the time when a patch was observed. The phase scintillation is higher near noon MUT than at other MUTs.
- This relationship is not as clearly visible in Figure 4(b) when the maximum value of the amplitude scintillation is plotted against the MUT.

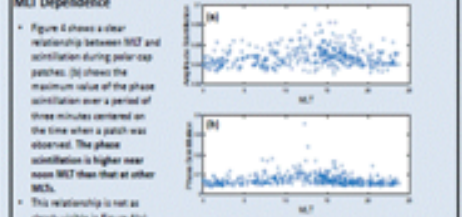


Figure 4: The 3 minute average of the amplitude ( $S_4$ ) and phase ( $\phi$ ) scintillation recorded at the patch center plotted as functions of MUT.

#### Event Analysis

- Despite there being no obvious increases in scintillation associated with polar cap patches statistically, there are times when scintillation indeed increases with patch presence. One example occurred on March 6, 2022, between 20:00 and 22:00 UT, when the phase scintillation increased to greater than 0.4 radians as shown by Figure 5 (a). Figure 5(b) shows the amplitude scintillation also increased slightly, "0.2, as shown by Figure 5.
- In this case, the daytime TEC increased around 20:35 UT as shown by Figure 6 (a), i.e., storm-enhanced density (SED), and the SED plume extended poleward into the polar cap (~10° TSS) when compared to the surrounding regions at about 20 TSS). Interestingly, the Resolute Bay receiver was just poleward of the cusp near the noon MLT.
- The maximum phase scintillation occurred at 20:37 UT, which coincides with the sharp density gradient there in Figure 6 (c). Figure 6(d) shows that the convection flow speed was very high (~900 m/s) in the region where the patch was observed.
- It is possible that polar cap patches that are severe enough with large electron density and sharp density gradient, as well as large convection flows to enhance scintillation significantly.
- The detailed instability mechanism is under investigation.

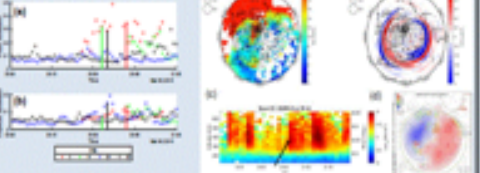


Figure 5: Phase ( $\phi$ ) and Amplitude ( $S_4$ ) scintillation from event files. The green line marks the first half prominence, the blue line marks the center, and the red line marks the second half prominence.

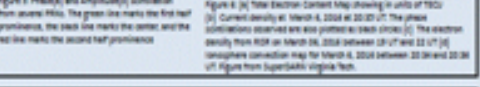


Figure 6: (a) Total Electron Content map (showing in units of TECU) (b) Current density at March 6, 2022 at 20:27 UT. The phase scintillations observed are also plotted as black circles. (c) The electron density from RGR on March 06, 2022 between 21:07 and 22:07 UT. (d) Convection flow map for March 6, 2022 between 20:30 and 22:30 UT. Figure from SuperMAG Virginia Tech.

#### Conclusion

Comparing the 3-minute averaged scintillation when a patch occurred to the scintillation averaged over one day, it was noted that there is not a significant difference between the two. There is no significant scintillation differences between the patch center and edges at Resolute Bay. Therefore, statistically there is no significant phase or amplitude scintillation increase associated with patches in the polar cap. However, there are 33 events where the phase scintillations are indeed enhanced when the difference between the daily average and the patch average was less than -0.05. Of these 33 events, 9 were during noon MUT (09-15 MUT), 8 were just before (7-9 MUT) or just after (15-18 MUT), 8 occurred just after 20 MUT. A patch itself may not be a sufficient condition for the scintillation to increase. It may cause scintillation if paired with other effects, such as sharp density gradient and fast convection flow. More quantitative work is needed to find out the exact instability mechanisms for patch to enhance scintillation.

#### Acknowledgments

The authors are grateful to the CHAN team for providing the CHAN data. The authors are also grateful to the SuperMAG team for providing the SuperMAG data. The authors are also grateful to the Resolute Bay team for providing the Resolute Bay data. The authors are also grateful to the RGR team for providing the RGR data. The authors are also grateful to the CHAN team for providing the CHAN data.

#### References

Ren, J., Cardenas-O'Toole, A., Zou, S., & Thayyil, J. (2022). Polar cap patches and ionospheric scintillation. *Journal of Geophysical Research: Space Physics*, 127, e2022JA026000. <https://doi.org/10.1029/2022JA026000>

Cardenas-O'Toole, A., Ren, J., Zou, S., & Thayyil, J. (2023). Ionospheric scintillation associated with polar cap patches. *Journal of Geophysical Research: Space Physics*, 128, e2023JA026000. <https://doi.org/10.1029/2023JA026000>

Zou, S., Cardenas-O'Toole, A., Ren, J., & Thayyil, J. (2023). Ionospheric scintillation associated with polar cap patches. *Journal of Geophysical Research: Space Physics*, 128, e2023JA026000. <https://doi.org/10.1029/2023JA026000>

Thayyil, J., Cardenas-O'Toole, A., Ren, J., & Zou, S. (2023). Ionospheric scintillation associated with polar cap patches. *Journal of Geophysical Research: Space Physics*, 128, e2023JA026000. <https://doi.org/10.1029/2023JA026000>

# Day 3: 2<sup>nd</sup> Prize

Harikrishnan Charuvil Asokan  
Leibniz-Institute of Atmospheric  
Physics, Rostock University,  
Kühlungsborn, Germany.

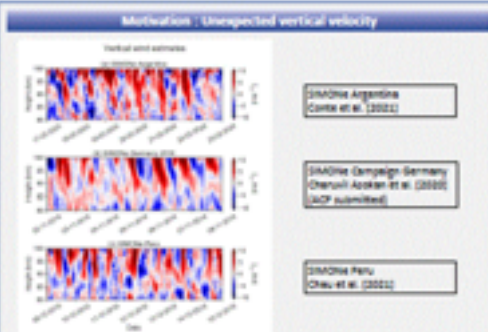
Title:

Validation of multistatic meteor radar analysis using realistic mesospheric dynamics from UA-ICON model: Reliability of gradients and vertical velocities

LEIBNIZ-INSTITUT FÜR ATMOSPÄRISCHE PHYSIK IAP Validation of multistatic meteor radar analysis using realistic mesospheric dynamics from UA-ICON model: Reliability of gradients and vertical velocities Leibniz

Harikrishnan Charuvil Asokan<sup>1,2</sup>, Jorge L. Chau<sup>3</sup>, Juan Federico Conte<sup>4</sup>, Raffaele Marino<sup>5</sup>, Juha Vierinen<sup>6</sup>, Gerd Baumgarten<sup>1</sup>, Sebastian Borchert<sup>1</sup>


**Motivation: Unexpected vertical velocity**



• IMADe Argentina Conte et al. (2021)  
• IMADe Campaign Germany Charuvil Asokan et al. (2020) ACP submitted  
• IMADe Peru Chau et al. (2021)

• Current tide structures and unexpected mean winds in the vertical velocity estimated from multistatic (specular meteor radar) networks motivated us to validate our methods by implementing IMADe geometry onto the UA-ICON high-resolution model.

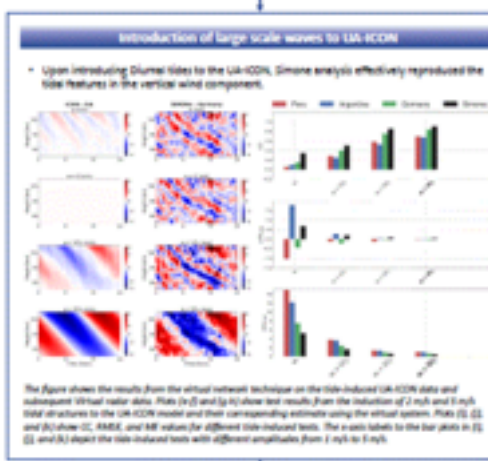
**validation through performance metrics**



• The validation analysis suggested that the mean wind estimation used in IMADe/IMADe networks works effectively.  
• The mean zonal, meridional winds and all the gradient terms showed good agreement in the analysis.  
• Vertical velocity estimates give unexpected high values without showing any tide features.

**Introduction of large scale waves to UA-ICON**

• Upon introducing diurnal tides to the UA-ICON, Simone analysis effectively reproduced the tide features in the vertical wind component.



The figure shows the results from the virtual network technique on the tide-induced UA-ICON data and subsequent Virtual radar data. Plots (a) and (b) show test results from the inclusion of 2 m/s and 5 m/s tidal structures to the UA-ICON model and their corresponding estimate using the virtual system. Plots (c) and (d) show CC, RMSE, and RM values for different tide-induced tides. The color labels in the bar plots in (c) and (d) refer to the tide-induced tides with different amplitudes from 1 m/s to 5 m/s.

**why should we validate meteor radar observations???**


- The background zonal and meridional winds from (specular meteor radars) (SMR) have been studied for a few decades, and they help understand the dynamics of the mesosphere and lower thermosphere. The estimation of these horizontal motions from SMRs is indispensable; however, vertical wind estimation has been challenging.
- In most of the meteor radar analysis, the vertical winds [w] are assumed to be zero [w=0], and it has been rationalized since SMRs have a large observation volume (circa 400 km in diameter).
- However, some of the recent analysis using multistatic SMR systems (as shown above) motivated us to look more carefully into the problem of vertical velocity determination from meteor radar. We posed the following questions: Is it possible to estimate vertical velocities and gradients using meteor radar? If yes, how accurate are these results?

**UA-ICON**

- ICOSphere Non-hydrostatic (ICON) general circulation model is a joint development of the Max Planck Institute for Meteorology (MPI-M) and the German Weather Service (DWD). Borchert, S. et al. (2018) extended the ICON to the upper atmosphere (ua-ICON).
- Resolution we used (nest 2):  
Latitude: 0.04° Longitude: 0.04°  
Time: 15 min Height: 1800 m (at M2 altitude)

The figure shows the latitude-longitude profile of vertical wind components at 80 km (resolution = 0.04°) at altitude and a single time frame (revolution) mid from UA-ICON.

**Virtual Meteor Radar: Block Diagram**



**Conclusions**

- The validation analysis based on the UA-ICON suggested that the SMR estimation techniques for mean zonal, meridional winds, and all the gradient terms work effectively.
- The variability of ± 1-2 m/s in the apparent vertical wind is due to horizontal wind inhomogeneities. However, it did not explain the tide features present in the actual multistatic SMR data.
- However, tide-induced study on the virtual radar showed that the current multistatic SMR networks and techniques could reproduce the tide features if they have an amplitude higher than ± 2 m/s.
- We encourage more scientific studies on M2 vertical winds.

**References**

- Charuvil Asokan et al. (2020), ACP, preprint.
- Chau, J. L. et al. (2021), Earth and Space Science, E. 202006001289.
- Conte, J. F. et al. 2021 Earth and Space Science, E. 202006001294.
- Charuvil Asokan et al. (2021), in preparation.

• Leibniz-Institute of Atmospheric Physics at the Rostock University, Kühlungsborn, Germany  
• Laboratoire de Mécanique des Fluides et d'Acoustique, CNRS, Ecole Centrale de Lyon, Université Claude Bernard Lyon 1, 69631 Saint-Etienne, France  
• Department of Physics and Technology, University of Tromsø, The Arctic University of Norway, Tromsø, Norway  
• Meteorwied, DLR/DFG at Wk, Germany

# Day 3: 1<sup>st</sup> Prize

Clayton Cantrall

University of Colorado, Boulder

Title:

Deriving column-integrated thermospheric temperature with the N<sub>2</sub> Lyman-Birge-Hopfield (2,0) band

**Deriving column-integrated thermospheric temperature with the N<sub>2</sub> Lyman-Birge-Hopfield (2,0) band**  
Clayton Cantrall<sup>1</sup>, Yoscha Merino<sup>2</sup>,  
<sup>1</sup>Department of Aerospace Engineering Sciences, University of Colorado Boulder

**Abstract:** We present a novel technique to derive thermospheric temperature from space-based disk observations of the ultraviolet Lyman-Birge-Hopfield (2,0) band. The technique uses a ratio of the emissions in two spectral channels that together span the Lyman-Birge-Hopfield (2,0) band to determine the change in limb-angle with respect to a change in the ambient temperature, T<sub>0</sub>.

**Motivation:** Past and present techniques to determine thermospheric temperature from LBRH emissions (Johnson et al. 2006; Johnson et al. 2013; Merino et al. 2013) have been effective but require matched LBRH measurements that require full nonlinear forward models that are hard to...  
1. Challenges in accurately quantification particularly representation error  
2. Increased representativeness due to differences in limb-angle and observed LBRH emission

**Goal:** Establish a robust observation type from LBRH limb-angle data...  
1. To enable to thermospheric temperature  
2. Provide a clear framework for accuracy quantification  
3. Facilitate representativeness error  
4. Can be used to both to advance the observation application and a clear standard

**LBRH temperature signal and two-channel ratio**

Figure 1 shows two panels, A and B. Panel A is a plot of 'Peak of LBRH Emission Profiles' vs 'Limb Angle (deg)'. It shows multiple curves for different limb angles, with a peak that shifts and changes shape as the limb angle increases. Panel B is a plot of 'Two-channel ratio' vs 'Limb Angle (deg)'. It shows several curves for different limb angles, generally showing a decreasing trend as the limb angle increases.

**Validation of two-channel ratio approach**

The two-channel ratio approach is validated using 10,000 GOLD Level 2 disk emission data. The efficacy of the approach is validated through comparison of the column-integrated temperature derived from GOLD Level 2 data (T<sub>0</sub>) with ratios of the GOLD Level 2 temperature profiles (T<sub>0</sub>/T<sub>1</sub>) as well as model temperatures based on Figure 3 from 100,000-400 km (T<sub>0</sub>) and two channel temperature distributions from synthetic distributions generated from 100,000 Whole Atmosphere Model (WAM) runs.

Figure 2 shows two panels, A and B. Panel A is a 4x4 grid of heatmaps showing 'T0/T1' vs 'Limb Angle (deg)'. The heatmaps show different patterns for different limb angles. Panel B is a plot of 'T0/T1' vs 'Limb Angle (deg)'. It shows several curves for different limb angles, generally showing a decreasing trend as the limb angle increases.

**Uncertainty quantification**

**Systematic measurement error (wavelength registration and resolution)**

Figure 3 shows two panels, A and B. Panel A is a plot of 'T0/T1' vs 'Limb Angle (deg)'. It shows several curves for different limb angles, generally showing a decreasing trend as the limb angle increases. Panel B is a plot of 'T0/T1' vs 'Limb Angle (deg)'. It shows several curves for different limb angles, generally showing a decreasing trend as the limb angle increases.

**Random (shot noise) and representativeness error (%) (10000 simulation population size)**

Figure 4 shows two panels, A and B. Panel A is a plot of 'T0/T1' vs 'Limb Angle (deg)'. It shows several curves for different limb angles, generally showing a decreasing trend as the limb angle increases. Panel B is a plot of 'T0/T1' vs 'Limb Angle (deg)'. It shows several curves for different limb angles, generally showing a decreasing trend as the limb angle increases.

**Further comparisons of T<sub>0</sub> to GOLD TDISE**

Figure 5 shows two panels, A and B. Panel A is a heatmap showing 'T0' vs 'Limb Angle (deg)'. It shows different patterns for different limb angles. Panel B is a heatmap showing 'T0' vs 'Limb Angle (deg)'. It shows different patterns for different limb angles.

**Conclusions**

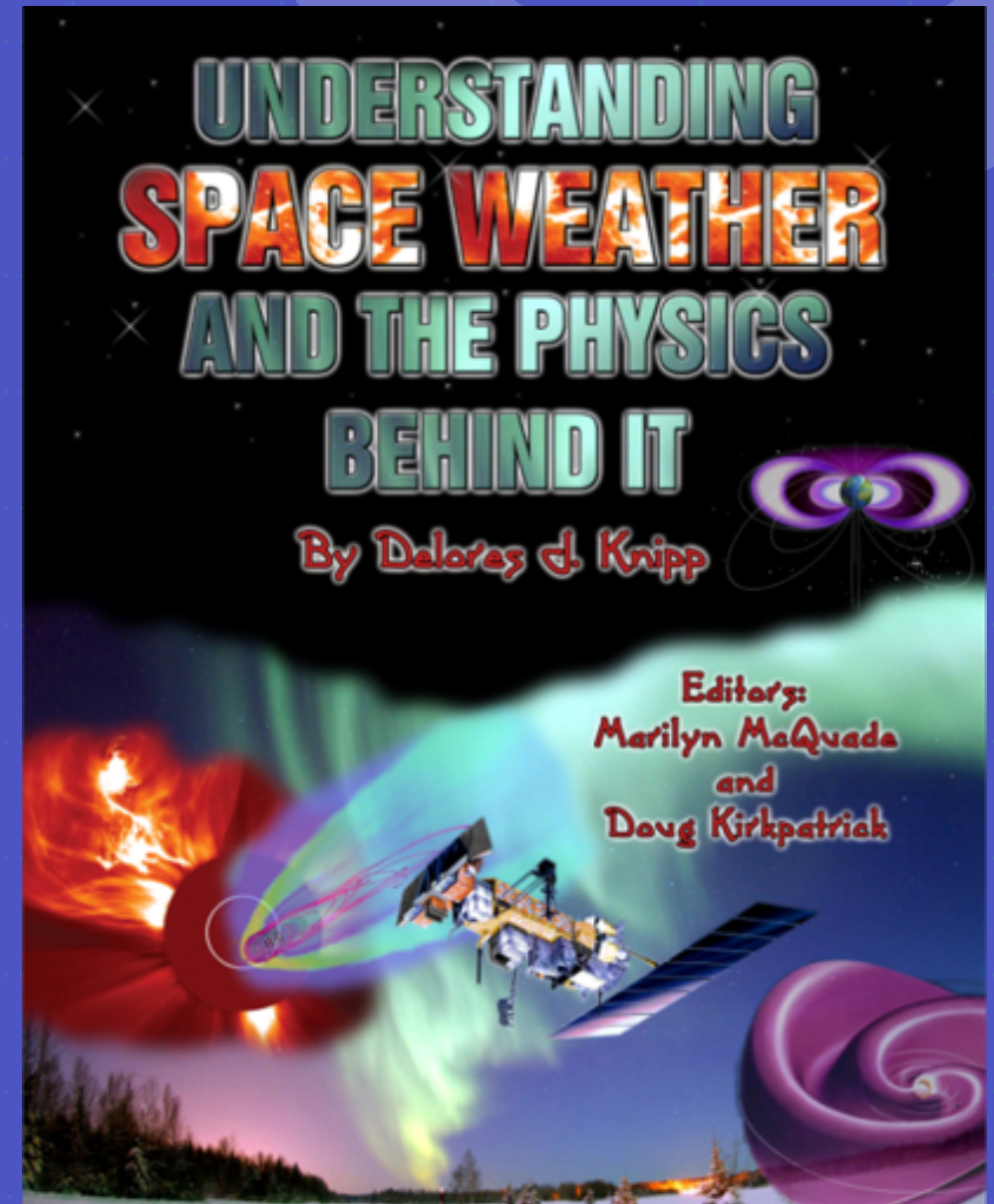
New technique to derive thermospheric temperature on the disk using two-channel ratio approach with 2,0 LBRH band  
Ratio approach simplifies forward model and effectively eliminates representativeness error due to limb angle emission and accuracy in WAM population size  
Ratio is only computed from GOLD Level 2 data  
Without use of a global information of temperature profile the derived temperature should be interpreted as a column-integrated quantity

**Quantified four dominant sources of uncertainty associated with the derived thermospheric temperature derivation:**  
Systematic measurement error (wavelength registration and resolution)  
Random measurement error (shot noise)  
Representativeness error (WAM relative population size)  
Random column-integrated emissions, T<sub>0</sub>, show general agreement with GOLD TDISE and MSIS temperatures and is a better proxy WAM temperature  
Significant differences between T<sub>0</sub> and TDISE as function of MS4 and MS4A

**References:** Johnson, B. et al., *Geophysical Research Letters*, 33, 2006; Johnson, B. et al., *Geophysical Research Letters*, 33, 2013; Merino, Y. et al., *Earth and Space Science*, 12, 2015; Merino, Y. et al., *Journal of Geophysical Research: Space Physics*, 2015

**Acknowledgments:** This work is supported by NASA grant 55024-12-1-0212 and NSF award ATM-1001361. High-performance computing support from Cheyenne (NSF CHE-0554306), was provided by the NCAR Computational and Information Systems Division. NCAR is supported by the National Science Foundation 0093079 from the National Science Foundation.

1st prize winner will receive an electronic copy of “Understanding Space Weather and the Physics behind it” by CSSC chair Delores Knipp



With thanks to Space Technology Series

Check out the winning CEDAR posters and all other posters even after the CEDAR workshop ends at

